Earth and Planetary Science Letters 474 (2017) 226–236

Contents lists available at ScienceDirect

Earth and Planetary Science Letters

www.elsevier.com/locate/epsl

Mapping the mantle transition zone beneath Hawaii from Ps receiver functions: Evidence for a hot plume and cold mantle downwellings

Matthew R. Agius [a,*], Catherine A. Rychert [a], Nicholas Harmon [a], Gabi Laske [b]

[a] Ocean and Earth Science, University of Southampton, United Kingdom
[b] Scripps Institution of Oceanography, University of California, San Diego, CA, USA

ARTICLE INFO

Article history:
Received 16 February 2017
Received in revised form 27 May 2017
Accepted 19 June 2017
Available online xxxx
Editor: R. Bendick

Keywords:
Hawaii
seismology
mantle plume
transition zone
mantle discontinuities
receiver functions

ABSTRACT

Hawaii is the archetypal example of hotspot volcanism. Classic plume theory suggests a vertical plume ascent from the core–mantle boundary to the surface. However, recently it has been suggested that the plume path may be more complex. Determining the exact trajectory of the Hawaiian plume seismic anomaly in the mantle has proven challenging. We determine P-to-S (Ps) receiver functions to illuminate the 410- and 660-km depth mantle discontinuities beneath the Hawaiian Islands using waveforms recorded on land and ocean-bottom seismometers, applying new corrections for tilt and coherence to the ocean bottom data. Our 3-D depth-migrated maps provide enhanced lateral resolution of the mantle transition zone discontinuities. The 410 discontinuity is characterised by a deepened area beneath central Hawaii, surrounded by an elevated shoulder. At the 660 discontinuity, shallow topography is located to the north and far south of the islands, and a deep topographic anomaly is located far west and east. The transition zone thickness varies laterally by ±13 km depth: thin beneath north-central Hawaii and thick farther away in a horseshoe-like feature. We infer that at 660-km depth a broad or possibly a double region of upwelling converges into a single plume beneath central Hawaii at 410-km depth. As the plume rises farther, uppermost mantle melting and flow results in the downwelling of cold material, down to at least 410 km surrounding the plume stem. This result in the context of others supports complex plume dynamics including a possible non-vertical plume path and adjacent mantle downwellings.

1. Introduction

In classical plume theory, mantle material rises vertically from the lowermost mantle to the surface of the Earth (Morgan, 1972). This theory was inspired by linear, age-progressive volcanic tracks trending in the direction of past and present plate motions such as the Hawaiian–Emperor seamount chain, which suggest that plate motion is over a fixed mantle upwelling (Wilson, 1963). Geochemical isotopes suggest that ocean-island volcanism may originate from a distinct mantle reservoir at the base of the mantle (e.g., Hofmann, 1997). Global seismic tomography studies image vertically elongated low-velocity anomalies associated with the ascending hot mantle through the entire lower mantle (e.g., Zhao, 2015; French and Romanowicz, 2015), with roots of an upwelling plume at the core–mantle boundary (e.g., Rost et al., 2005). However, the exact dimensions and trajectory of the plumes through the mantle are debated, and greater complexity has been suggested. Precise imaging is challenging given the hypothesised narrow size of the plumes (Morgan, 1972) in comparison with the wavelengths of the seismic waves to image these features. For instance, plume ascent might not be vertical, perhaps deflected by mantle wind (Steinberger and O'Connell, 1998), and the dimensions of the plume might change from the lower mantle to the upper mantle (e.g., Richards et al., 1989; Tosi and Yuen, 2011). Due to a significant decrease in sensitivity, seismic anomalies associated with a certain temperature anomaly are also vastly decreased in the lower mantle, hampering reliable tracking of a seismic anomaly from the upper mantle through the transition zone into the lower mantle. And in turn, the exact relationship of the plume ascent in the lower mantle to the upper mantle is not well-understood. This is where mapping variations in mantle transition zone (TZ) thickness are useful. Elevated plume temperatures are predicted to deepen the 410- and shallow the 660-km depth mantle discontinuities thinning the transition zone (e.g., Deuss et al., 2013).

Hawaii is the archetypal example of hotspot volcanism. Low seismic velocities (and thus by proxy high thermal anomalies)

* Corresponding author at: National Oceanography Centre, University of Southampton, Waterfront Campus, European Way, Southampton SO14 3ZH, United Kingdom.
E-mail address: matthew.agius@soton.ac.uk (M.R. Agius).

http://dx.doi.org/10.1016/j.epsl.2017.06.033

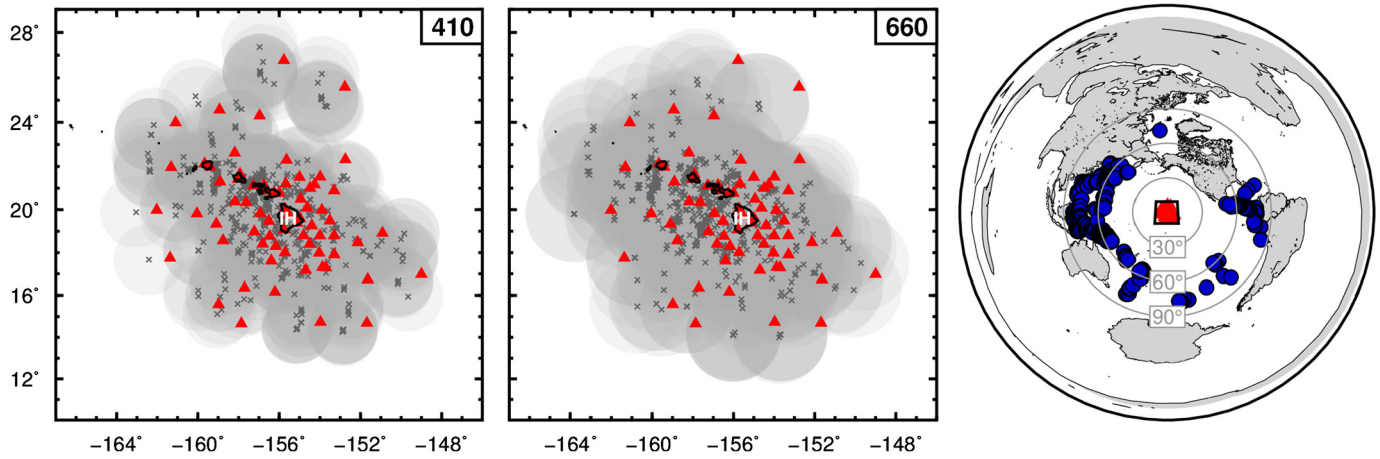

Fig. 1. Maps showing the distribution of piercing points at 410-km depth (left frame) and 660-km depth (central frame), and the corresponding stations (triangles) and earthquake sources (closed blue circles, right frame) used in this study. In the left two frames, semi-transparent grey shades are the corresponding Fresnel sensitivity zone for each piercing point. In the right frame, concentric circles show epicentral distance away from the study area. IH: Island of Hawaii.

have been imaged in the uppermost mantle beneath Hawaii (e.g., Laske et al., 2011), extending into the lower mantle (Wolfe et al., 2009, 2011; Cheng et al., 2015), and possibly down to the core–mantle boundary (e.g., Lei and Zhao, 2006; French and Romanowicz, 2015). Measurements for the mantle transition zone thickness using seismic receiver functions (RF) show areas that have considerable thinning and other areas with significant thickening (e.g., Li et al., 2000). A thinned transition zone has been located beneath different areas, with different thicknesses and lateral dimensions. For example, a thinner transition zone has been identified west–southwest of the Hawaiian islands, (Li et al., 2000; Collins et al., 2002), beneath the islands (Shen et al., 2003), and east of Hawaii close to the Island of Hawaii (Huckfeldt et al., 2013). It is unclear whether the main topographic contribution for the thinned TZ is from an updoming of the 660-km discontinuity (Li et al., 2000), a depressed 410, or a combination of a depressed 410 and an updoming 660 (Wölbern et al., 2006; Huckfeldt et al., 2013). Seismic tomographic images of a deflected plume within the TZ have been interpreted to be vertically tilted SE–NW (Wolfe et al., 2009; Cheng et al., 2015) and SW–NE (Wölbern et al., 2006). Each of these possibilities has geodynamic implications as to whether a plume is ponding below, within, or above the transition zone, and also has implications on the trajectory of the plume to the surface. It is thus essential for our understanding to discriminate between these possibilities. Here we use P-to-S receiver functions determined from ocean bottom seismometers (OBSs) and permanent land stations to image variations in the 410- and 660-km depth discontinuities beneath Hawaii and constrain the trajectory and dimensions of the plume. We apply improved signal processing techniques on the OBS data to enhance signal to noise and enhance imaging across the region.

2. Data and method

We made use of publicly available data from a combination of permanent and temporary, land and ocean-bottom broadband seismometers across the Hawaiian archipelago. Many of the stations have been deployed at different times through different projects such as the Hawaiian Plume–Lithosphere Undersea Mantle Experiment (PLUME, Laske et al., 2009, 2011) and the Ocean Seismic Network Pilot Experiment (OSNPE site OSN-1, Collins et al., 2001). Waveforms of teleseismic earthquakes with a magnitude greater than $M_w = 5.5$ and with an epicentral distance to the stations between 35° and 80° were downloaded from the Incorporated Research Institutions for Seismology (IRIS) data management centre. The seismic stations and earthquakes used in this study are shown in Fig. 1. The earthquakes are listed in Supplementary Table 1.

Preprocessing of the waveforms included: decimating the seismograms to 10 samples per second, band-pass filtering between 0.05–0.2 Hz, and rotating the horizontal components to the radial and transverse components using orientation corrections determined from the polarization of teleseismic surface waves (Rychert et al., 2013). Where unavailable, orientations were determined from P-wave polarization analysis. The chosen frequency range for the filtering was selected following tests on the data for both land and ocean stations. Supplementary Fig. 1 shows examples of different frequency ranges tested. Additional preprocessing to the ocean stations included the removal of tilt noise on the vertical components (Crawford and Webb, 2000) and the removal of compliance noise, as a result of pressure variations associated with infra-gravity waves (Bell et al., 2015).

Each recorded earthquake was manually inspected and a distinct P-wave arrival within ±5 seconds of the theoretical arrival was selected. This signal was deconvolved from the radial component using the extended multitaper frequency domain deconvolution technique (Helffrich, 2006; Rychert et al., 2013) to produce a receiver function, which is essentially a band limited impulse response of a P-to-S (Ps) phase conversion as a result of a seismic velocity discontinuity located beneath the station. The deconvolution effectively removes the effects of the instrument response and source spectra. A positive amplitude RF phase indicates a velocity increase with depth, whereas a negative amplitude indicates a velocity decrease. Data from OBS stations have higher noise levels, as expected, and thus require careful selection. We inspected each RF, eliminated unstable deconvolutions (pure ringing), and only selected cases with a clear Ps phase amplitude of $\gtrsim 0.2$ for the Moho discontinuity and $\gtrsim 0.1$ for 410 and 660 discontinuities (P410s and P660s, respectively). Theoretical arrival times of the three Ps phases acted as a guide for the selected arrival time.

In practice, a strong Moho phase was generally present in the RFs. However, given that P410s and P660s conversions arrive far into the coda, it was common that one phase was clear, while the other was obscured by ringing. In an effort to maximise the potential use of as many waveforms as possible, individual data sets were selected for the P410s and the P660s. These waveforms had to have a good Moho phase and a good signal for the respective phase. In an interactive process, the P wave was re-examined and the receiver function reviewed where necessary.

Each receiver function is migrated to depth, correcting for the sphericity of the Earth. We use a crust-corrected, one-dimensional

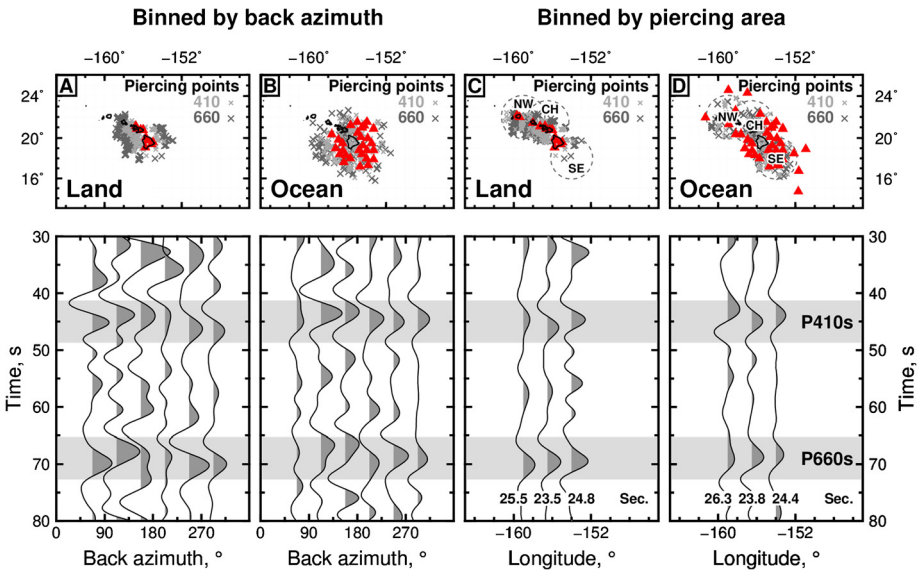

Fig. 2. Comparison of receiver functions from land and ocean stations. The averaged waveforms are deconvolved P-to-S receiver functions with respect to time, bandpass filtered between 0.05 to 0.2 Hz, and without elevation corrections. Averaged waveforms from P410s and P660s data sets are merged together. A, B: Receiver functions binned by earthquake-station back azimuth from North, with stations (triangles) centred on/round the Island of Hawaii. C, D: Receiver functions binned by piercing-point areas of 2° radius (dashed circles) beneath Northwest Hawaii (NW), Central Hawaii (CH) and Southeast Hawaii (SE). Light and dark grey crosses are piercing points at the 410 and 660 mantle discontinuities, respectively. Grey shaded bands indicate the expected time arrival of the P410s and P660s phases, respectively. Dark grey filled parts of the wiggles represent the positive amplitude of the receiver function. Frames A, B and C, D compare the receiver functions between land and ocean stations, the latter tend to have earlier peaks because of their negative elevation. Seconds in the bottom right frames are the peak time differences between P660s and P410s. Individual deconvolved waveforms for Central Hawaii are shown in Supplementary Fig. 1.

(1-D) preliminary reference Earth model (PREM, Dziewonski and Anderson, 1981). We use average crustal thicknesses for land (17 km) and ocean (7 km) from the local study of Leahy et al. (2010), with typical body-wave velocities (CRUST1.0, Laske et al., 2013). Station elevation corrections are applied such that discontinuity depths are with respect to sea level. The migrated receiver functions are then back projected along the theoretical ray path and stacked onto a three-dimensional (3-D) grid (e.g., Rychert et al., 2013) that has a lateral spacing of 1° by 1° and a 1-km depth vertical spacing. The grid is then smoothed with a radius corresponding to the Fresnel zone of the waveform determined by $\sqrt{(\frac{\lambda}{2}+d)^2-d^2}$, where λ is the wavelength and d is the depth (Fig. 1). Because of the separate selection of the P410s and P660s phases, we generate two 3-D grids, which are then merged into a single grid using a linear weighting between 410- to 660-km depth of the grids.

In total, we used 932 waveforms recorded at 14 land and 55 ocean-bottom seismometers. The P410s data set comprised of 682 waveforms whereas the P660s data set comprised of 630 waveforms. The piercing points from the respective data sets are shown in Fig. 1.

2.1. Receiver function uncertainties

We tested the degree to which the ocean stations agreed with the land stations. In other words, given the noisiness of the ocean, whether or not the OBS contributed any signal at all by evaluating the land and ocean station separately. In one case we focused on the stations on/surrounding the Island of Hawaii and binned by back azimuth (Fig. 2A and B). In another test, we focused on three areas (northwest, central and southeast Hawaii, Fig. 2C and D). The receiver functions from the land and ocean compare well. Those from ocean stations have peaks that are slightly shifted to an earlier time because of the negative elevation. Central Hawaii is characterized by a clearly increased delay time of the P410s interface in contrast to the adjacent northwest and southeast Hawaii areas (Fig. 2C and 2D). The P660s, however, has fewer variations hinting that it is relatively flat along this profile. Individual waveforms from land and ocean stations for central Hawaii are shown in Supplementary Fig. 1.

Uncertainties for the receiver function can be estimated with bootstrap resampling. This provides a statistical assessment of the signal coherence and stability from randomly selected traces within a sample (e.g., Efron and Tibshirani, 1986). As an example, we bin depth-migrated receiver functions that have both phases (P410s and P660s) within the same area, average the receiver function traces, and calculate the standard deviation from the bootstrap. The three selected areas include both land and ocean stations, and sample places that have a high and a low number of waveforms (Fig. 3). The amplitude of the uncertainty (two standard deviations) tends to increase with the decrease of waveforms, though maintaining a clear pulse at the expected phase arrival time.

3. Results

Our maps for the mantle transition zone discontinuities provide an extended lateral coverage than previously mapped. The tilt and compliance corrections combined with the extended multitaper frequency domain deconvolution approach, and careful data selection allowed us to map the discontinuities at a high resolution over a broad area of more than 10° diameters beneath and surrounding Hawaii.

Variations at the mantle transition zone interfaces are observed directly from the deconvolution (Fig. 2), individually as P410s and P660s as well as from their delay time differences (P660s–P410s). Central Hawaii has less delay time difference than its adjacent regions (23.5–23.8 s), indicating significant thinning there. The topographies are mapped on vertical and horizontal cross-sections extracted from the 3-D depth migrated receiver functions (Figs. 4 and 5). The 410-km depth mantle discontinuity (d410) is characterised by a deepened area beneath central Hawaii ($\lesssim$ 10 km

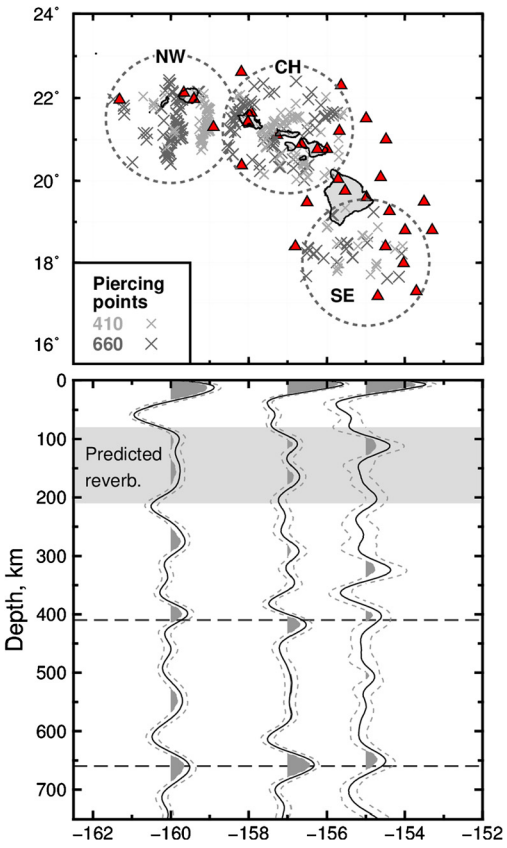

Fig. 3. Depth migrated receiver functions for Northwest Hawaii (NW), Central Hawaii (CH) and Southeast Hawaii (SE). Each stack (solid wiggle) represents the bin average for the respective area shown on the map above (dashed circles), using a crust-corrected PREM velocity model (Dziewonski and Anderson, 1981). Dashed wiggles are two standard deviations estimated from bootstrap analysis using 100 randomly selected subsets from within the respective bins. Grey shaded band indicates predicted crustal reverberations. The waveforms used are members of both P410s and the P660s data sets and are from land and ocean stations (triangles). Dark grey filled parts of the wiggles represent the positive amplitude of the receiver function. Horizontal dashed lines mark the 410- and 660-km depths.

depth, >400 km wide), surrounded by a ring-like elevated shoulder ($\lesssim 13$ km depth). At the d660, the discontinuity appears shallow beneath the north to south-east of the Hawaiian Islands ($\lesssim 5$ km depth), however, the shallowest topography is located farther north and south of the islands ($\lesssim 12$ km depth, Fig. 5). The d660 map is also marked by large areas of deep topography at the far west and east of the islands.

The thickness of the transition zone, determined from the depth difference between the d660 and d410, shows an anomalous thin zone beneath north-central Hawaii ($\lesssim 13$ km thin, Fig. 5) surrounded by a thick shoulder ($\lesssim 13$ km thick). The horseshoe-like configuration of the TZ beneath Hawaii consists of an approximately $4° \times 7°$ wide SW–NE oriented inner thin zone (west of the Island of Hawaii), and an outer 2° wide thick zone.

4. Discussion

A key signature for a thermally elevated mantle transition zone is its reduced thickness. The two dominant discontinuities that mark the transition zone are generally defined by olivine phase transformations that take place at pressures equivalent to 410- and 660-km depth. At high temperatures, the 410 phase transition of olivine to wadsleyite ($\alpha \rightarrow \beta$, Katsura and Ito, 1989) takes place at higher pressure (greater depth), whereas at the 660, the transition of ringwoodite to perovskite and magnesiowüstite ($\gamma \rightarrow pv + mw$, e.g., Ito et al., 1990) takes place at a lower pressure (shallower depth) (e.g., Bina and Helffrich, 1994; Deuss et al., 2013). Changes in the depth of each respective discontinuity and the corresponding transition zone thickness have been observed globally seismically using techniques such as receiver functions (e.g., Lawrence and Shearer, 2006), SS precursors (e.g., Lawrence and Shearer, 2008; Houser, 2016) and PP precursors studies (e.g., Deuss, 2009). These studies, as well as regional studies of the Pacific Ocean (e.g., Cao et al., 2011; Zheng et al., 2015), suggest thinning over very broad areas, several hundred kilometres in diameter, either beneath (e.g., Cao et al., 2011), or surrounding (e.g., Houser, 2016), or several hundred kilometres west (e.g., Lawrence and Shearer, 2008) or east (e.g., Zheng et al., 2015) of Hawaii, rather than a distinct 100–200 km anomaly beneath Hawaii. The advantage of receiver functions is a smaller Fresnel zone ($\approx$200 km) that allows detection of smaller scale features, than, in contrast, to SS precursors which have Fresnel zones of $>$1000 km radius (e.g., Lawrence and Shearer, 2008; Deuss, 2009).

Here we focus on robust features of the TZ thickness beneath Hawaii, test the effect of a plume in the background velocity model, compare the topographic heterogeneity of each interface with seismic velocities at their respective depths, and compare qualitatively the temperature anomalies with those from geodynamic numerical models.

4.1. The thickness of the mantle transition zone

Measurements for the mantle transition zone thickness using seismic land stations located on Hawaii show areas that have considerable thinning and other areas with significant thickening (e.g., Li et al., 2000). Different studies have, however, inconsistent results about the dimension, amplitude and location of the thickness anomaly. A thin transition zone has been identified west–southwest of the Hawaiian islands, (Li et al., 2000; Collins et al., 2002), beneath the islands (Shen et al., 2003), and east of Hawaii close to the Island of Hawaii (Huckfeldt et al., 2013). Thickness estimates vary: from -50 to -30 km (Li et al., 2000), -30 ± 15 km (Collins et al., 2002) and from -35 to $+15$ km (Huckfeldt et al., 2013), whereas Wölbern et al. (2006) estimated that the d410 depth increases by 45 km and the d660 shallows by 60 km (although the bending of each interface is not vertically aligned). In general, the magnitude of our thinning is at the lower-end of these local studies and are also within the ranges of regional SS precursors studies (e.g., Cao et al., 2011; Zheng et al., 2015).

Our maps agree well with the lateral features of areas identified earlier that have a thin/thick mantle transition zone. For example, the thin region west–southwest of the Island of Hawaii determined by Li et al. (2000) covers an area where we image with thinning. Similarly, an area west of Hawaii with considerable thickening matches with our study (Fig. 7D). The magnitudes of the P660s–P410s delays in this area are in good agreement, greater than 26 s by Li et al. (2000) and 25.5–26.3 s in our study (Fig. 2C and 2D). Beneath central Hawaii we find a thinned transition zone (23.5–23.8 s) also in the range of Li et al. (2000), who reports a broader differential time (23–26 s). For comparison, we calculate the theoretical transition zone thickness from the P660s–P410s delay times of 23–26 s from Li et al. (2000) using a PREM velocity-depth model and a reference epicentral distance of 60° (Fig. 7D).

We find that the thinnest area is located beneath central Hawaii (-13 km) surrounded by a horseshoe-like thick transition zone ($+13$ km, Fig. 5). The thinned area probably represents the location of the plume stem, whereas the outer thicker areas indicate colder regions. The implications of these features on the plume dynamics are discussed in Section 4.4.

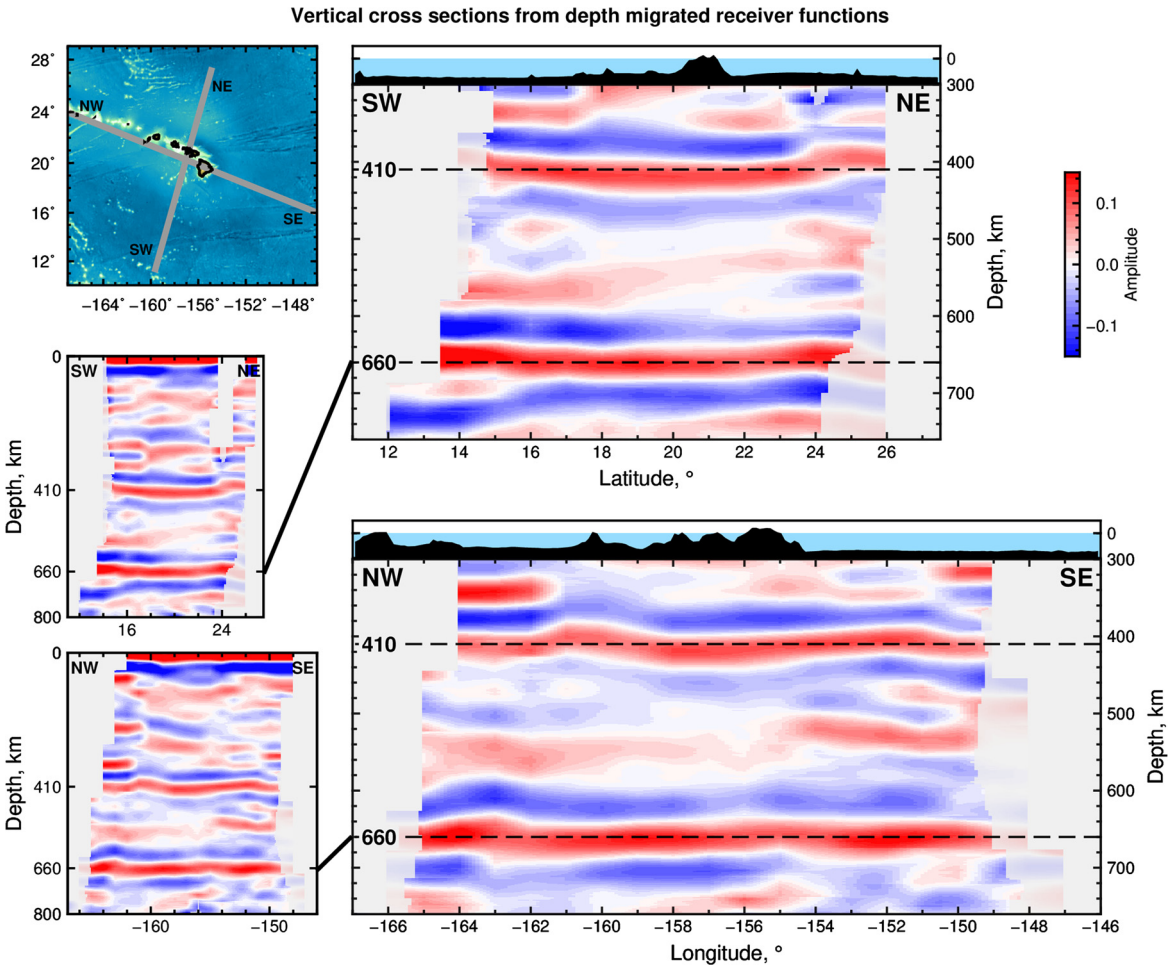

Fig. 4. Vertical cross-sections through the 3-D depth migrated receiver functions calculated using a crust-corrected PREM velocity model (Dziewonski and Anderson, 1981). Red and blue shades represent positive and negative amplitudes saturated at ±0.15, respectively. The image resolution is from a 1° by 1° latitude–longitude grid. Semi-transparent shades represent poorly constrained areas due to a low number of traces (< 5). Top left: Map showing the location of the two vertical cross-sections SW–NE and NW–SE. Bottom left frames: The entire depth cross sections from the surface down to 800-km depth. Right: Zoomed cross sections between 300–760 km depth. Dashed black lines mark the 410- and 660-km depths. The corresponding bathymetry and elevation are shown above each cross-section. Depths are with respect to sea level.

4.1.1. Velocity model tests on transition zone thickness

The background velocity model used for migration is critical to determine the accurate depth of discontinuities. In the case of the mantle transition zone thickness, the differential discontinuity depths of the d660 and d410 should minimize errors from unknown anomalies above 410-km depth. However, this is only the case when there is no lateral heterogeneity within the TZ. We test for different hypothetical models by varying the background velocities and identify robust features (Fig. 6). For each test the shear velocity is perturbed (dV_S) while the compression velocity is kept fixed to the crust-corrected PREM (Dziewonski and Anderson, 1981), thus varying the V_P/V_S ratio. The magnitude of the dV_S is based on the PLUME tomography of Wolfe et al. (2009).

Reducing V_S by a magnitude of 1% in our 1-D migration model results in shifting each interface to a shallow depth, which consequently thins the transition zone (Fig. 6B). Beneath the Hawaiian Islands the TZ is in the range of 10–20 km thinner, whereas the thicker periphery is less than 5 km thicker. In the second test (Fig. 6C) we tested a 3-D migration model that has a hot plume represented by a vertical column with a −1% V_S in the location of the thinnest TZ (Fig. 6A). This anomaly affects only ray paths traversing through the column volume. In this test, the TZ within the plume is thinned by 5–15 km, whereas the thickest TZ located southeast off the Island of Hawaii is 15 km. The third test is a complex configuration of a wider slow (−0.5% V_S) vertical plume encircled by a 'cold', faster outer tube (+0.5% V_S, Fig. 6D) representing the broad inner and outer thin/thick areas (Fig. 6A). This test yielded similar TZ thicknesses to those in the previous test of a single column (Fig. 6C), but with some areas of thicker TZ being broader.

A robust pattern of a central thin transition zone surrounded by areas of increased thickness is noticeable across all four models (Fig. 6) giving us confidence that our interpreted features are not artefacts of shallow mantle velocity heterogeneity. In published cases where the transition zone thickness determined from a 1-D velocity model was compared with that derived from a 3-D velocity model inferred from seismic tomography, the large-scale lateral features persisted in both models, albeit with variable TZ thickness anomaly magnitudes (e.g., Lee et al., 2014; Liu et al., 2015; Jenkins et al., 2016), consistent with our testing.

4.2. Shear-velocities at the 410 and 660 discontinuities

Shear-wave velocities are sensitive to temperature. A higher temperature reduces the V_S, whereas a lower temperature increases the velocity (e.g., Anderson, 1987). Seismic studies inferred from surface waves (Laske et al., 2011), body waves (Wolfe et al., 2009) or a combination of both (e.g., Cheng et al., 2015; French and Romanowicz, 2015) have imaged focused regions of low *S* velocities beneath Hawaii that are thus likely to represent the plume conduit.

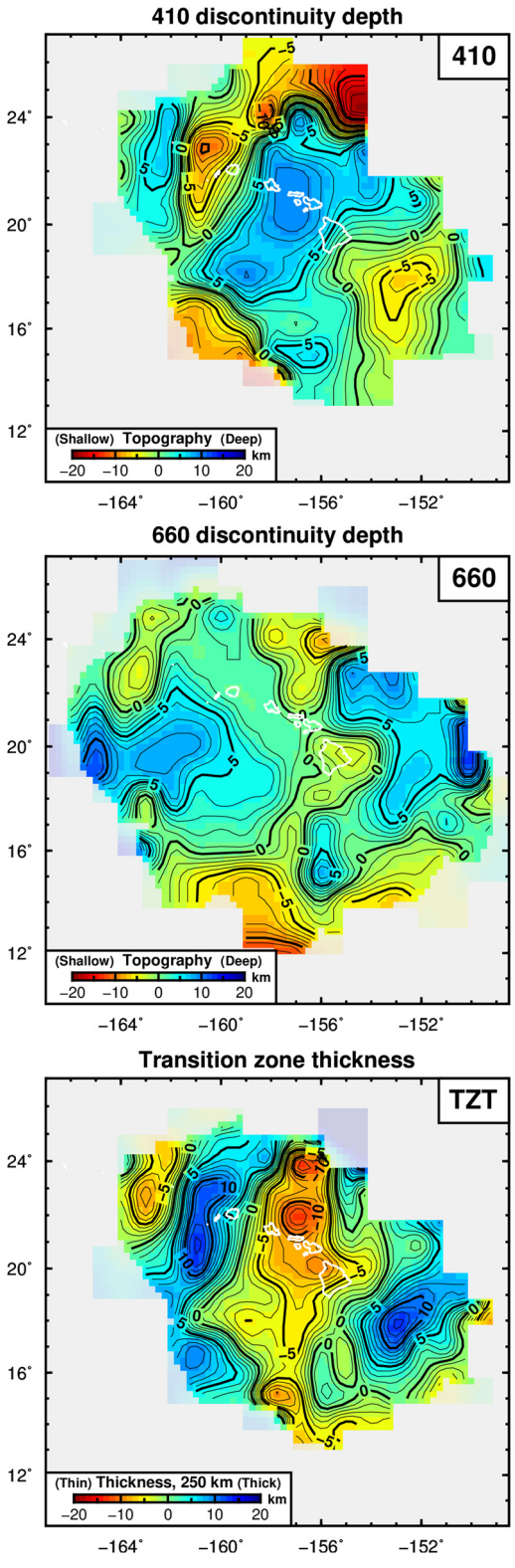

Fig. 5. Horizontal cross sections from the 3-D depth migrated receiver functions calculated using a crust-corrected PREM velocity model (Dziewonski and Anderson, 1981). Top: Topography of the 410 mantle discontinuity. Middle: Topography of the 660 mantle discontinuity. Bottom: Mantle transition zone thickness (TZT). Thick black contours are at an interval of 5 km. The image resolution is from a 1° by 1° latitude–longitude grid. Semi-transparent shades represent poorly constrained areas due to a low number of traces (< 5).

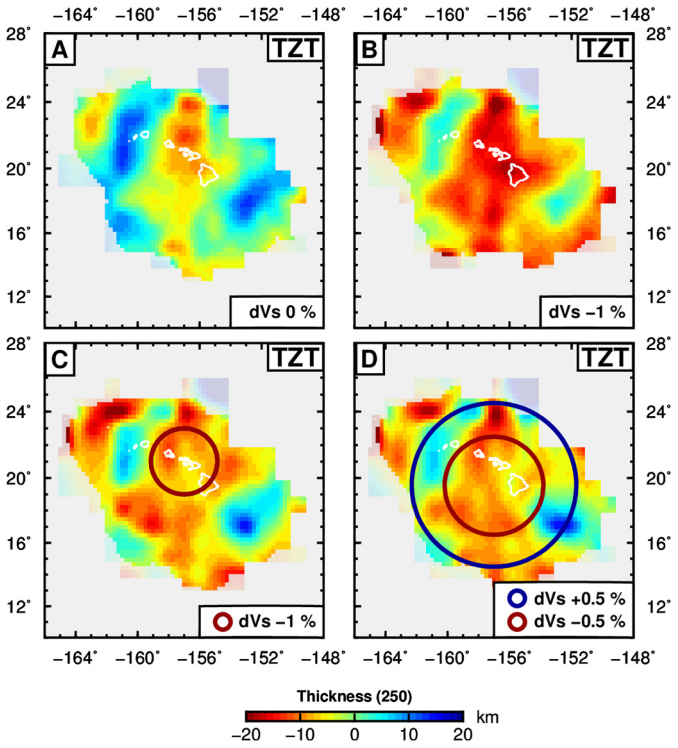

Fig. 6. Tests on the TZ thickness from hypothetical plume models in the migration model. The shear velocity is perturbed (dV_S) while the compression velocity is kept fixed to the crust-corrected PREM (Dziewonski and Anderson, 1981). A: The preferred model using the crust-corrected PREM. B: Reduced V_S by −1% throughout. C: A hypothetical plume made of a vertical column (red circle) with reduced V_S (−1%) in comparison to PREM. D: Two concentric tubes define a plume with an inner volume reduced S velocity of −0.5% and an outer layer with a higher V_S of +0.5%. This configuration is designed to represent the broader features mapped in A. Semi-transparent shades represent poorly constrained areas due to a low number of traces.

We compared our discontinuity maps with the V_S tomography of Wolfe et al. (2009) and Cheng et al. (2015). The latter shows less agreement with the topographies. For example, at 600-km depth, Cheng et al. (2015) have high-velocity anomalies beneath central Hawaii, whereas at the d660 we see relatively shallow topography. Similarly, the area west of Hawaii has low V_S in areas where the d660 is deeper. In contrast, the V_S anomalies of Wolfe et al. (2009) coincide with the changes of the d410 and d660 topographies, respectively. At 410-km depth, a low-velocity anomaly beneath central Hawaii coincides with the depressed discontinuity there, whereas areas with higher or relatively higher V_S are located near shallow topography (Fig. 7A). Respectively, at 660, areas with a low-velocity anomaly coincide with shallow discontinuity and vice versa (Fig. 7B). In the French and Romanowicz (2015) model, the low V_S anomaly at 660-km depth is located beneath the Hawaiian Islands and bends westwards as it reaches 410-km depth, in contrast to our image.

The relationship of shallow/deep topography at the respective discontinuities with high/low V_S and, by proxy, with temperature too, follows the expected behaviour determined by positive and negative Clapeyron slopes (e.g., Bina and Helffrich, 1994; Deuss et al., 2013). This good agreement with shear velocities gives us added confidence in our results, particularly with establishing a more accurate lateral structure and delineation of a plume at these two depths. For example, at 660-km depth, two distinct anomalies at north-central and south-southeastern Hawaii are characterised by a shallow interface and a low-velocity anomaly, adding evidence of high temperatures at this depth and strengthening arguments for the presence of a hot source below.

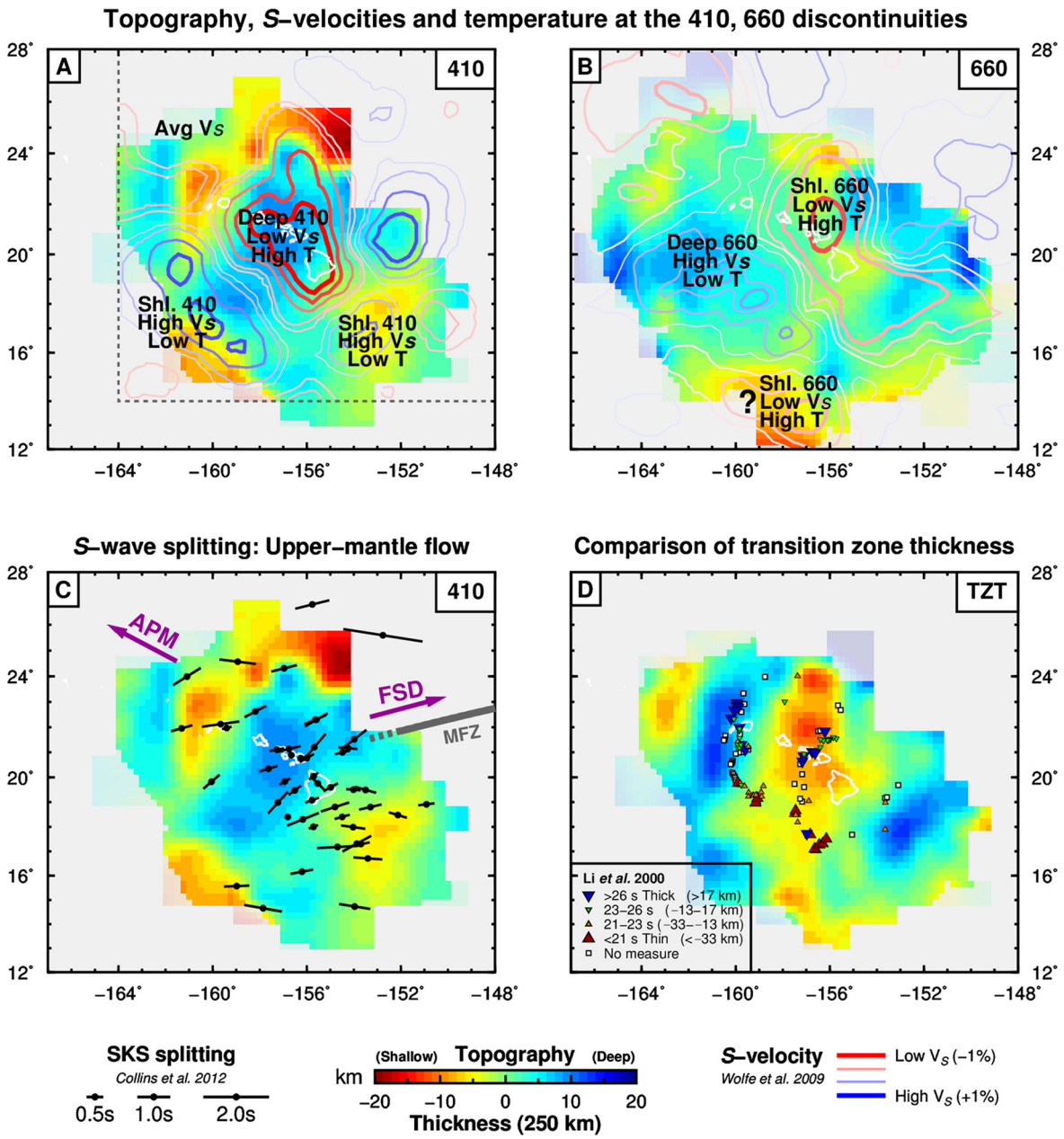

Fig. 7. Comparison of the topography at the 410 and 660 mantle discontinuities and mantle transition zone thickness (TZT) with other studies. Top: Horizontal cross sections from the depth migrated receiver functions compared with *S* velocity from *S*-wave arrival times (Wolfe et al., 2009). Red and blue contours represent low and high *S*-velocity anomalies, respectively. A: Low shear velocities at 400-km depth coincide with a deep 410 interface. Shallow areas are characterised by relatively faster V_S. Dotted grey box indicates the area modelled by *S* waves. B: Low shear velocities at 600-km depth coincide with a shallow 660 interface, whereas deep 660 interfaces are in areas of relatively higher V_S. Shear-velocity anomalies are a good proxy for temperature changes (e.g., Karato, 1993). C: Fast directions of shear-wave splitting of teleseismic *SKS* waves (Collins et al., 2012) show deflections round the contour of the deeper 410 discontinuity. APM: Absolute plate motion. FSD: Fossil spread direction parallel to the Molokai Fracture Zone (MFZ). D: Comparison of mantle transition zone thickness from the depth migrated receiver functions (this study) with the P-to-S converted seismic phases by Li et al. (2000). The colour code of the P660s piercing points represent the differential times between phases P660s–P410s and indicate thinner (red and orange triangles) and thicker (blue inverted triangles) mantle transition zone thickness.

Similarly, the coincidental high *S* velocities with shallow/deep topographies at the 410/660 km discontinuities give evidence of cooler temperatures present at these depths. These low temperatures are likely to be an integral part of the plume dynamics, possibly a result of cold downwelling material (e.g., Moore et al., 1998; Wolfe et al., 2009).

4.3. Temperature estimates

We determine three estimates for the mantle transition zone 'hot' and 'cold' temperature anomalies using relationships of temperature with thickness and with discontinuity depths. We neglect effects of composition and assume that perturbations to the discontinuity depths are due to temperature-induced changes alone. Furthermore, these are lower limits because local anomalies may be smaller than the area sensitive by the receiver functions.

Temperature anomalies based on TZ thickness are inferred from a joint study of P660s–P410s differential times determined from Ps receiver functions with shear speeds determined from a regional tomography (-0.13 ± 0.07 km/K, Lebedev et al., 2002). A ± 13 km thickness variation results in a temperature range of ± 100 K (Fig. 8). These temperatures may be an underestimate in the case that the thinning or thickening is not vertically aligned.

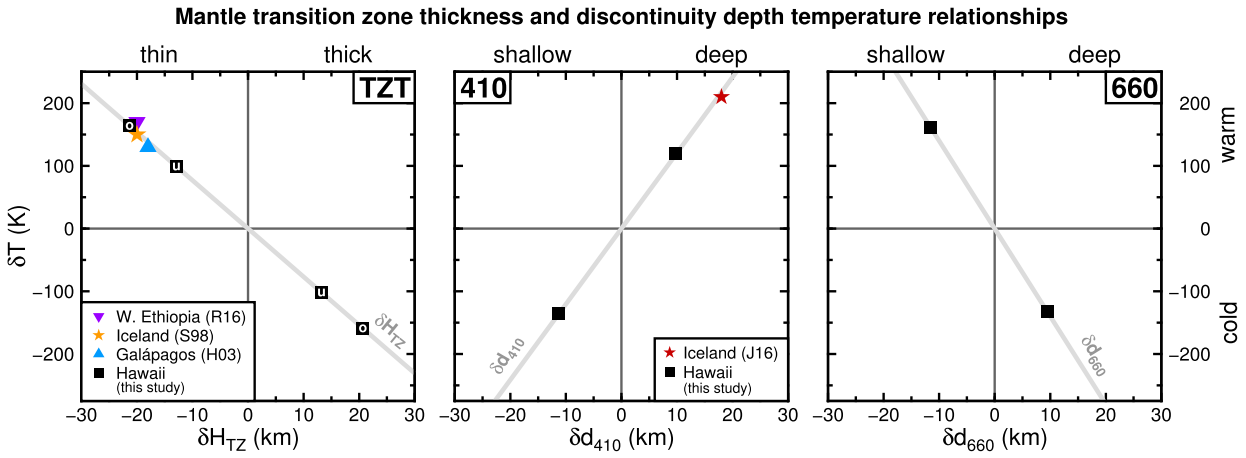

Fig. 8. Estimates of hot and cold temperature anomalies with respect to the TZ thickness and to the depth variations of the 410 (d410) and 660 (d660) mantle discontinuities. Left frame: Grey line is the temperature–TZ thickness relationship H_{TZ} (-0.13 ± 0.07 km/K, Lebedev et al., 2002). Different symbols represent values for other places: Western Ethiopian Plateau (Reed et al., 2016, inverted purple triangle), Iceland (Shen et al., 1998, orange star), and Galápagos (Hooft et al., 2003, blue triangle). All estimates are from Ps receive functions and are based on similar inferences. Black squares: This study. Letters mark (u)nder- and (o)ver-estimated temperatures based on the TZ thickness 'vertical' alignment of the d410 and d660 discontinuities. Centre frame: Grey line is the Clapeyron slope for the d410 (+2.9 MPa/K, Bina and Helffrich, 1994). Red star: Estimate for Iceland from Jenkins et al. (2016). Right frame: Grey line is the Clapeyron slope for d660 (-2.5 MPa/K, Ye et al., 2014). (For interpretation of the references to colour in this figure legend, the reader is referred to the web version of this article.)

Considering the deepest and the shallowest areas of d410 and d660 to determine an overestimate results in +165 K and −160 K, respectively (Fig. 8). These are the preferred temperature estimates because TZ thickness is generally considered more robust in the presence of velocity heterogeneity in the upper mantle.

For completeness, we obtain two temperature estimates from the discontinuity depth changes using experimental relationships based on pressure and mineral phase transitions. A gradient of +2.9 MPa/K at the d410 discontinuity (Bina and Helffrich, 1994) and −2.5 MPa/K at the d660 discontinuity (Ye et al., 2014), with depth changes in the range of +10 and −11 km depth respectively, implies an excess temperature of +119 K and +162 K, respectively (Fig. 8). Estimates for the cooler temperatures are about −135 K for both the d410 and d660. These temperature estimates will vary if different derivatives are applied; a wide range of values exists for the Clapeyron slopes, from 1.5–2.9 MPa/K for the phase transition at d410 (e.g., Akaogi et al., 1989; Bina and Helffrich, 1994) and from −4.0 to −2.0 MPa/K at the d660 (e.g., Ito et al., 1990; Bina and Helffrich, 1994). Here, we note a good agreement between the temperature estimates from each single discontinuity and the range of temperature estimates from TZ thickness (Fig. 8).

Other considerations that may have a role in determining the temperature at the phase boundaries are the presence of water and post-garnet phase transformation (e.g., Litasov et al., 2013). If water is present, then one would expect a combination of low shear velocity with a shallow d410 and a depressed d660 (e.g., Houser, 2016), however, this is not observed (Fig. 7). In the case of the post-garnet transition at the d660, the phase transformation changes the Clapeyron slope from anti-correlated phase boundaries to correlated boundaries, resulting in a positive Clapeyron slope at the 660 km discontinuity (e.g., Jenkins et al., 2016). Our results show no obvious combination of high temperature (low V_S) and correlated depressed d410 and d660 (Fig. 7).

In summary, the thermal anomalies are in the range from +100 to +165 K and from −100 to −160 K, with average values for the hot and cold areas of about ±135 K. These temperatures are similar to estimates derived from peak-to-peak S velocity. Assuming a $\partial ln V_S / \partial T$ value of -1.3×10^{-4} (Karato, 1993), a ±1.5% V_S anomaly at 400- and a ±1% at 600-km depth (Wolfe et al., 2009) infers a thermal change of ±115 K and ±77 K, respectively. Our hot temperatures are lower than those published for Hawaii using similar approaches. For example, Li et al. (2000) suggest that a 30–50 km thinned TZ yields a 200–350 K warmer than the surrounding mantle. Others propose 325 K and 375 K from a ∼30 km and 45 km depressed d410 (Huckfeldt et al., 2013; Wölbern et al., 2006, respectively), and 400 K determined for a reported 60 km thinned TZ (Collins et al., 2002).

Our estimates compare well with temperatures reported for other hotspot regions such as Galápagos (130 K, Hooft et al., 2003), Iceland (150 K, Shen et al., 1998) and the Western Ethiopian Plateau (170 K, Reed et al., 2016)—all using similar inferences used here (Fig. 8). In this regard, note that these regions have similar mantle transition zone thicknesses. Our estimates are also in agreement with temperatures ranges based on petrological studies (Herzberg and Gazel, 2009). Temperatures exceeding 200 K have recently been reported for Iceland (Jenkins et al., 2016, Fig. 8, red star). There, the correlated d410 and d660 topographies suggest that the 660-km depth discontinuity is controlled by a garnet phase transition. We do not observe such a correlation and our observations indicate that temperatures are unlikely to be high enough for the d660 to reach the post garnet stage (Hirose, 2002).

4.4. Plume dynamics

One of the major findings of the PLUME experiment was not only the focused low-velocity anomaly associated with a plume conduit but also the presence of high-velocity regions extending down several hundred kilometres (Wolfe et al., 2009). The high velocities are interpreted as cold curtains of downwelling, mechanically eroded lithospheric material (e.g., Moore et al., 1998). Geodynamic models suggest this could be related to small-scale convection (Ballmer et al., 2011). Our observations fit well into these previous observations and models. The temperature anomalies and distance of the cooler regions encircling the Hawaiian Islands at the 410-km depth coincide with the numerical model of Ballmer et al. (2011) (Fig. 9).

A similar ring-like feature has been observed beneath Iceland (Jenkins et al., 2016), however, the authors argue that this may be an artefact where the anomalous upper mantle is affected across a wider area at 660-km than at 410-km depth. A major advantage to our dataset is the larger station distribution—roughly 1,250 × 1,400 km in contrast to 350 × 500 km area for Iceland, reducing the drawback of having ray paths focused to a central island. The same area on an interface is illuminated from different

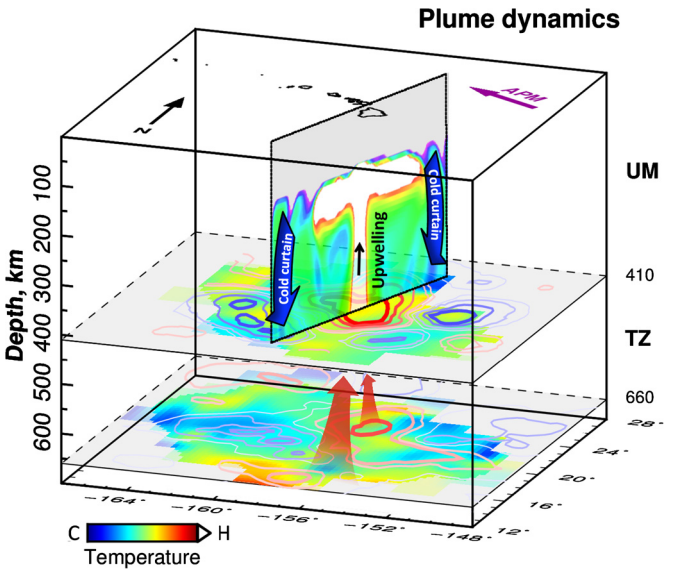

Fig. 9. 3-D schematic showing plume dynamics within the TZ and upper mantle beneath Hawaii inferred from the 410 and 660-km depth interfaces, shear-wave velocities and geodynamic modelling. Colour shades on each cross-section are indicative of hot and cold temperature anomalies. The horizontal cross sections are inferred from the d410 and d660 topography. The contours are inferred from shear velocities (Wolfe et al., 2009). The vertical cross section is from the geodynamic numerical model of Ballmer et al. (2011), perpendicular to the absolute plate motion (APM). At 660-km depth, a broad or possibly a double region of upwelling (red arrows) converges into a single plume located beneath Central Hawaii. As the plume rises (black arrow), uppermost mantle melting and flow may result in the downwelling of cold material (blue arrows), sinking down to at least 410-km depth (e.g., Ballmer et al., 2011).

station-earthquake trajectories diminishing projection biases from only one direction (Fig. 1).

The plume lateral and vertical flow may have been detected by seismic anisotropy (Collins et al., 2012). Here we plot the splitting fast directions and time analysed from *SKS* waves on top of the d410 map for comparison (Fig. 7C). The amplitude of the splitting time appears to diminish beneath Central and Southeast Hawaii, with the stations having some of the smallest splitting times located on top of deep d410. An explanation for this is that strong vertical variations such as from a rising plume can generate an apparent small splitting (Collins et al., 2012; Ito et al., 2014). Another observation is that many of the fast directions located within the deep d410 have their azimuth rotated slightly anti-clockwise from WSW–ENE (parallel to the fossil spread direction, FSD) to SW–NE. The change in direction may be the result of a complex vertical ascent, deflecting from Central Hawaii at 410-km depth towards the south at 150–100 km depth, where a low shear velocity is located (Laske et al., 2011).

We interpret our results based on a combination of observations, starting from 660-km depth, heading upwards. At the 660, the shallow topography together with the low shear velocities indicate that a broad or possibly a double region of hot upwelling converges into a single plume (Wolfe et al., 2009), located beneath Central Hawaii at the deepened 410 discontinuity and the thinnest transition zone (Figs. 5 and 9). The southern opening of the horseshoe-like shallow areas surrounding the deeper d410 and the lack of a thick TZ there suggests that a hot feed is present from the south below the d410. As the plume rises farther from beneath Central Hawaii at 410 km to 150–100 km depth it deflects towards the south, west of the Island of Hawaii (Laske et al., 2011; Collins et al., 2012; Rychert et al., 2013), and then to the Island of Hawaii at the surface. Altogether, these results present strong evidence that the plume deflects with depth every few hundred kilometres. During the ascent uppermost mantle melting and flow may result in the downwelling of cold material, sinking down to at least ∼ 400-km depth (e.g., Ballmer et al., 2011), or deeper to 660 km. The presence of cold material is confirmed by the high shear velocities (Wolfe et al., 2009) and by the shallow d410 and deep d660 mantle phase transitions observed here.

5. Conclusion

We map the mantle transition zone discontinuities beneath Hawaii from seismic receiver functions using a combination of land and ocean-bottom seismometers. The d410 beneath central Hawaii is characterised by a deepened area, surrounded by a horseshoe-like elevated shoulder. At the d660, the greatest shallow topography is located north and far south of the islands, and with areas of deep topography at the far west and east of the islands. The deep and shallow perturbations at the d410 and d660 coincide with the high and low *S* velocities inferred from tomography. The TZ thickness varies laterally by ±13 km depth: thin beneath north-central Hawaii and thick farther away. The thin zone is approximately $4^\circ \times 7^\circ$ wide, whereas the outer thick circumference is 2° wide. Specific tests for the TZ thickness using hypothetical plume models show that the large-scale hot and cold features are robust.

High and low thermal anomalies are in the range of +100 to +165 K and −100 to −160 K, with average values of about ±135 K. Our excess temperatures are similar to those of other hotspot regions such as Iceland, Galápagos and other ocean islands. The temperatures are unlikely to be high enough to reach the post garnet stage at the d660. The location and temperature of the cooler regions at the d410 are similar to those predicted by geodynamic models, described as cold curtains (Fig. 9).

The combination of our results with other seismic studies add increasing evidence that the plume dynamics are different from the classic model of a fixed plume that ascends vertically, but instead, the plume deflects with depth every few hundred kilometres. At 660-km depth, a broad or possibly a double region of upwelling converges into a single plume beneath Central Hawaii at 410-km depth. As the plume rises farther, uppermost mantle melting and flow results in the downwelling of cold material, down to at least 410-km depth surrounding the plume stem.

Acknowledgements

The authors thank two anonymous reviewers for insightful comments that helped to improve this paper. The facilities of Incorporated Research Institutions for Seismology (IRIS) Data Services, and specifically the IRIS Data Management Center, were used for access to waveforms, related metadata, and/or derived products used in this study. IRIS Data Services are funded through the Seismological Facilities for the Advancement of Geoscience and EarthScope (SAGE) Proposal of the National Science Foundation under Cooperative Agreement EAR-1261681. The PLUME project, which provided the majority of the OBS records for this study, was funded through NSF grant OCE-0002470. Global Seismographic Network (GSN) is a cooperative scientific facility operated jointly by the IRIS, the United States Geological Survey (USGS), and the National Science Foundation (NSF), under Cooperative Agreement EAR-1261681. Rychert, Harmon and Agius were supported by funding from the Natural Environment Research Council (NE/M003507/1) and the European Research Council (GA 638665).

Appendix A. Supplementary material

Supplementary material related to this article can be found online at http://dx.doi.org/10.1016/j.epsl.2017.06.033.

References

Akaogi, M., Ito, E., Navrotsky, A., 1989. Olivine-modified spinel–spinel transitions in the system Mg_2SiO_4–Fe_2SiO_4: calorimetric measurements, thermochemical calculation, and geophysical application. J. Geophys. Res. 94, 15671–15685. http://dx.doi.org/10.1029/JB094iB11p15671.

Anderson, D.L., 1987. Thermally induced phase changes, lateral heterogeneity of the mantle, continental roots, and deep slab anomalies. J. Geophys. Res. 92, 13968–13980. http://dx.doi.org/10.1029/JB092iB13p13968.

Ballmer, M.D., Ito, G., van Hunen, J., Tackley, P.J., 2011. Spatial and temporal variability in Hawaiian hotspot volcanism induced by small-scale convection. Nature 4, 457–460. http://dx.doi.org/10.1038/ngeo1187.

Bell, S.W., Forsyth, D.W., Ruan, Y., 2015. Removing noise from the vertical component records of ocean-bottom seismometers: results from year one of the cascadia initiative. Bull. Seismol. Soc. Am. 105, 300–313. http://dx.doi.org/10.1785/0120140054.

Bina, C.R., Helffrich, G., 1994. Phase-transition Clapeyron slopes and transition zone seismic discontinuity topography. J. Geophys. Res. 99, 15853–15860.

Cao, Q., van der Hilst, R.D., de Hoop, M.V., Shim, S.H., 2011. Seismic imaging of transition zone discontinuities suggests hot mantle west of Hawaii. Science 332, 1068–1071. http://dx.doi.org/10.1126/science.1202731.

Cheng, C., Allen, R.M., Porritt, R.W., Ballmer, M.D., 2015. Seismic constraints on a double-layered asymmetric whole-mantle plume beneath Hawaii. In: Hawaiian Volcanoes: From Source to Surface, pp. 19–34.

Collins, J.A., Vernon, F.L., Orcutt, J.A., Stephen, R.A., 2002. Upper mantle structure beneath the Hawaiian swell: constraints from the ocean seismic network pilot experiment. Geophys. Res. Lett. 29, 1522. http://dx.doi.org/10.1029/2001GL013302.

Collins, J.A., Vernon, F.L., Orcutt, J.A., Stephen, R.A., Peal, K.R., Wooding, F.B., Spiess, F.N., Hildebrand, J.A., 2001. Broadband seismology in the oceans: lessons from the ocean seismic network pilot experiment. Geophys. Res. Lett. 28, 49–52. http://dx.doi.org/10.1029/2000GL011638.

Collins, J.A., Wolfe, C.J., Laske, G., 2012. Shear wave splitting at the Hawaiian hot spot from the PLUME land and ocean bottom seismometer deployments. Geochem. Geophys. Geosyst. 13. http://dx.doi.org/10.1029/2011GC003881.

Crawford, W.C., Webb, S.C., 2000. Identifying and removing tilt noise from low-frequency ($\leq$0.1 Hz) seafloor vertical seismic data. Bull. Seismol. Soc. Am. 90, 952–963. http://dx.doi.org/10.1785/0119990121.

Deuss, A., 2009. Global observations of mantle discontinuities using SS and PP precursors. Surv. Geophys. 30, 301–326. http://dx.doi.org/10.1007/s10712-009-9078-y.

Deuss, A., Andrews, J., Day, E., 2013. Seismic Observations of Mantle Discontinuities and Their Mineralogical and Dynamical Interpretation. John Wiley & Sons, Ltd., pp. 295–323. Chapter 10.

Dziewonski, A.M., Anderson, D.L., 1981. Preliminary reference Earth model. Phys. Earth Planet. Inter. 25, 297–356. http://dx.doi.org/10.1016/0031-9201(81)90046-7.

Efron, B., Tibshirani, R., 1986. Bootstrap methods for standard errors, confidence intervals, and other measures of statistical accuracy. Stat. Sci. 1, 54–75.

French, S.W., Romanowicz, B., 2015. Broad plumes rooted at the base of the Earth's mantle beneath major hotspots. Nature 525, 95–99. http://dx.doi.org/10.1038/nature14876.

Helffrich, G., 2006. Extended-time multitaper frequency domain cross-correlation receiver-function estimation. Bull. Seismol. Soc. Am. 96, 344–347. http://dx.doi.org/10.1785/0120050098.

Herzberg, C., Gazel, E., 2009. Petrological evidence for secular cooling in mantle plumes. Nature 458, 619–622. http://dx.doi.org/10.1038/nature07857.

Hirose, K., 2002. Phase transitions in pyrolitic mantle around 670-km depth: implications for upwelling of plumes from the lower mantle. J. Geophys. Res. 107. http://dx.doi.org/10.1029/2001JB000597.

Hofmann, A.W., 1997. Mantle geochemistry: the message from oceanic volcanism. Nature 385, 219–229. http://dx.doi.org/10.1038/385219a0.

Hooft, E.E., Toomey, D.R., Solomon, S.C., 2003. Anomalously thin transition zone beneath the Galápagos hotspot. Earth Planet. Sci. Lett. 216, 55–64.

Houser, C., 2016. Global seismic data reveal little water in the mantle transition zone. Earth Planet. Sci. Lett. 448, 94–101. http://dx.doi.org/10.1016/j.epsl.2016.04.018.

Huckfeldt, M., Courtier, A.M., Leahy, G.M., 2013. Implications for the origin of Hawaiian volcanism from a converted wave analysis of the mantle transition zone. Earth Planet. Sci. Lett. 373, 194–204. http://dx.doi.org/10.1016/j.epsl.2013.05.003.

Ito, E., Akaogi, M., Topor, L., Navrotsky, A., 1990. Negative pressure–temperature slopes for reactions forming $MgSiO_3$ Perovskite from Calorimetry. Science 249, 1275–1278. http://dx.doi.org/10.1126/science.249.4974.1275.

Ito, G., Dunn, R., Li, A., Wolfe, C.J., Gallego, A., Fu, Y., 2014. Seismic anisotropy and shear wave splitting associated with mantle plume–plate interaction. J. Geophys. Res. 119, 4923–4937. http://dx.doi.org/10.1002/2013JB010735.

Jenkins, J., Cottaar, S., White, R., Deuss, A., 2016. Depressed mantle discontinuities beneath Iceland: Evidence of a garnet controlled 660 km discontinuity? Earth Planet. Sci. Lett. 433, 159–168. http://dx.doi.org/10.1016/j.epsl.2015.10.053.

Karato, S.i., 1993. Importance of anelasticity in the interpretation of seismic tomography. Geophys. Res. Lett. 20, 1623–1626. http://dx.doi.org/10.1029/93GL01767.

Katsura, T., Ito, E., 1989. The system Mg_2SiO_4–Fe_2SiO_4 at high pressures and temperatures: precise determination of stabilities of olivine, modified spinel, and spinel. J. Geophys. Res. 94, 15663–15670. http://dx.doi.org/10.1029/JB094iB11p15663.

Laske, G., Collins, J.A., Wolfe, C.J., Solomon, S.C., Detrick, R.S., Orcutt, J.A., Bercovici, D., Hauri, E.H., 2009. Probing the Hawaiian hot spot with new broadband ocean bottom instruments. Eos Trans. AGU 90, 362–363. http://dx.doi.org/10.1029/2009EO410002.

Laske, G., Markee, A., Orcutt, J.A., Wolfe, C.J., Collins, J.A., Solomon, S.C., Detrick, R.S., Bercovici, D., Hauri, E.H., 2011. Asymmetric shallow mantle structure beneath the Hawaiian Swell–evidence from Rayleigh waves recorded by the PLUME network. Geophys. J. Int. 187, 1725–1742. http://dx.doi.org/10.1111/j.1365-246X.2011.05238.x.

Laske, G., Masters, G., Ma, Z., Pasyanos, M., 2013. Update on CRUST1.0 – a 1-degree global model of Earths crust. In: Geophys. Res. Abstr., p. 2658.

Lawrence, J.F., Shearer, P.M., 2006. A global study of transition zone thickness using receiver functions. J. Geophys. Res. 111, b06307. http://dx.doi.org/10.1029/2005JB003973.

Lawrence, J.F., Shearer, P.M., 2008. Imaging mantle transition zone thickness with SdS-SS finite-frequency sensitivity kernels. Geophys. J. Int. 174, 143. http://dx.doi.org/10.1111/j.1365-246X.2007.03673.x.

Leahy, G.M., Collins, J.A., Wolfe, C.J., Laske, G., Solomon, S.C., 2010. Underplating of the Hawaiian Swell: evidence from teleseismic receiver functions. Geophys. J. Int. 183, 313–329. http://dx.doi.org/10.1111/j.1365-246X.2010.04720.x.

Lebedev, S., Chevrot, S., van der Hilst, R.D., 2002. Seismic evidence for olivine phase changes at the 410- and 660-kilometer discontinuities. Science 296, 1300–1302. http://dx.doi.org/10.1126/science.1069407.

Lee, S.H., Rhie, J., Park, Y., Kim, K.H., 2014. Topography of the 410 and 660 km discontinuities beneath the Korean Peninsula and southwestern Japan using teleseismic receiver functions. J. Geophys. Res. 119, 7245–7257. http://dx.doi.org/10.1002/2014JB011149.

Lei, J., Zhao, D., 2006. A new insight into the Hawaiian plume. Earth Planet. Sci. Lett. 241, 438–453. http://dx.doi.org/10.1016/j.epsl.2005.11.038.

Li, X.H., Kind, R., Priestley, K., Sobolev, S.V., Tilmann, F., Yuan, X., Weber, M., 2000. Mapping the Hawaiian plume conduit with converted seismic waves. Nature 405, 938–941. http://dx.doi.org/10.1038/35016054.

Litasov, K.D., Ohtani, E., Sano, A., 2013. Influence of Water on Major Phase Transitions in the Earth's Mantle. American Geophysical Union, pp. 95–111.

Liu, Z., Niu, F., Chen, Y.J., Grand, S., Kawakatsu, H., Ning, J., Tanaka, S., Obayashi, M., Ni, J., 2015. Receiver function images of the mantle transition zone beneath {NE} China: new constraints on intraplate volcanism, deep subduction and their potential link. Earth Planet. Sci. Lett. 412, 101–111. http://dx.doi.org/10.1016/j.epsl.2014.12.019.

Moore, W.B., Schubert, G., Tackley, P., 1998. Three-dimensional simulations of plume–lithosphere interaction at the Hawaiian Swell. Science 279, 1008–1011. http://dx.doi.org/10.1126/science.279.5353.1008.

Morgan, W.J., 1972. Deep mantle convection plumes and plate motions. Am. Assoc. Pet. Geol. Bull. 56, 203–213.

Reed, C., Gao, S., Liu, K., Yu, Y., 2016. The mantle transition zone beneath the Afar Depression and adjacent regions: implications for mantle plumes and hydration. Geophys. J. Int. 205, 1756–1766. http://dx.doi.org/10.1093/gji/ggw116.

Richards, M.A., Duncan, R.A., Courtillot, V.E., 1989. Flood basalts and hot-spot tracks: plume heads and tails. Science 246, 103–107. http://dx.doi.org/10.1126/science.246.4926.103.

Rost, S., Garnero, E.J., Williams, Q., Manga, M., 2005. Seismological constraints on a possible plume root at the core–mantle boundary. Nature 435, 666–669.

Rychert, C.a., Laske, G., Harmon, N., Shearer, P.M., 2013. Seismic imaging of melt in a displaced Hawaiian plume. Nat. Geosci. 6, 657–660. http://dx.doi.org/10.1038/ngeo1878.

Shen, Y., Solomon, S.C., Bjarnason, I.T., Wolfe, C.J., 1998. Seismic evidence for a lower-mantle origin of the Iceland plume. Nature 395, 62–65. http://dx.doi.org/10.1038/25714.

Shen, Y., Wolfe, C.J., Solomon, S.C., 2003. Seismological evidence for a mid-mantle discontinuity beneath Hawaii and Iceland. Earth Planet. Sci. Lett. 214, 143–151. http://dx.doi.org/10.1016/S0012-821X(03)00349-2.

Steinberger, B., O'Connell, R.J., 1998. Advection of plumes in mantle flow: implications for hotspot motion, mantle viscosity and plume distribution. Geophys. J. Int. 132, 412–434. http://dx.doi.org/10.1046/j.1365-246x.1998.00447.x.

Tosi, N., Yuen, D.A., 2011. Bent-shaped plumes and horizontal channel flow beneath the 660 km discontinuity. Earth Planet. Sci. Lett. 312, 348–359. http://dx.doi.org/10.1016/j.epsl.2011.10.015.

Wilson, J.T., 1963. A possible origin of the Hawaiian Islands. Can. J. Phys. 41, 863–870.

Wölbern, I., Jacob, A.W.B., Blake, T.A., Kind, R., Li, X., Yuan, X., Duennebier, F., Weber, M., 2006. Deep origin of the Hawaiian tilted plume conduit derived from receiver functions. Geophys. J. Int. 166, 767–781. http://dx.doi.org/10.1111/j.1365-246X.2006.03036.x.

Wolfe, C.J., Solomon, S.C., Laske, G., Collins, J.A., Detrick, R.S., Orcutt, J.A., Bercovici, D., Hauri, E.H., 2009. Mantle shear-wave velocity structure beneath the Hawaiian hot spot. Science 326, 1388–1390. http://dx.doi.org/10.1126/science.1180165.

Wolfe, C.J., Solomon, S.C., Laske, G., Collins, J.A., Detrick, R.S., Orcutt, J.A., Bercovici, D., Hauri, E.H., 2011. Mantle P-wave velocity structure beneath the Hawaiian hotspot. Earth Planet. Sci. Lett. 303, 267–280. http://dx.doi.org/10.1016/j.epsl.2011.01.004.

Ye, Y., Gu, C., Shim, S.H., Meng, Y., Prakapenka, V., 2014. The postspinel boundary in pyrolitic compositions determined in the laser-heated diamond anvil cell. Geophys. Res. Lett. 41, 3833–3841. http://dx.doi.org/10.1002/2014GL060060.

Zhao, D., 2015. Hotspots and mantle plumes. In: Multiscale Seismic Tomography. Springer Japan, Tokyo, pp. 1–304, 1963.

Zheng, Z., Ventosa, S., Romanowicz, B., 2015. High resolution upper mantle discontinuity images across the Pacific Ocean from SS precursors using local slant stack filters. Geophys. J. Int. 202, 175. http://dx.doi.org/10.1093/gji/ggv118.